

# High resolution near-IR spectroscopy of FGK stars

Daniel Thaagaard Andreasen

March 29, 2017



*To Linnea, Henriette, and Rico  
For always supporting me*



# CONTENTS

<b>Contents</b>	<b>iii</b>
<b>Abstracts</b>	<b>v</b>
<b>List of Figures</b>	<b>vi</b>
<b>List of Tables</b>	<b>vi</b>
<b>1 Introduction</b>	<b>1</b>
1.1 Planet host stars . . . . .	3
1.2 Atmospheric parameters . . . . .	3
<b>2 Theory</b>	<b>5</b>
2.1 Stellar structure . . . . .	5
2.2 Stellar atmosphere . . . . .	7
2.2.1 Atmosphere models . . . . .	8
2.2.2 Radiative transfer code - MOOG . . . . .	9
2.2.3 The equivalent width . . . . .	9
2.2.3.1 Temperature dependence . . . . .	10
2.2.3.2 Pressure dependence . . . . .	10
2.2.3.3 Abundance dependence . . . . .	12
2.2.3.4 Microturbulence . . . . .	12
2.3 Stellar parameters for FGK stars - the EW method . . . . .	14
2.3.1 Line list and atomic data . . . . .	15
2.3.2 Measuring EW . . . . .	16
2.3.3 Excitation and ionization balance . . . . .	17
<b>Bibliography</b>	<b>21</b>



## ABSTRACTS

## LIST OF FIGURES

2.1	An absorption line centred at $\lambda_0$ normalised at the flux level $F_c$ . The area of the absorption line to the left is equal to the blue shaded area in the rectangle to the right with width EW. . . . .	10
2.2	The EW for a Fe I and Fe II line with increasing $T_{\text{eff}}$ . The two lines have similar EW in the Sun and are found in the optical part of the spectrum. . . . .	11
2.3	<i>Upper panel:</i> Curve of growth for same Fe II used in Figure 2.2 on page 11 for four different $\log g$ values. Here it is the weak lines mostly affected by the change in $\log g$ . <i>Lower left panel:</i> Synthetic spectra of the same line. The colour scale is the same. <i>Lower right:</i> The abundance for the line at different $\log g$ . A strong correlation (0.40) is seen. . . . .	13
2.4	<i>Upper panel:</i> Curve of growth of the same Fe I line as used in Figure 2.2 on page 11. Four points are marked which is shown in the <i>lower panel</i> as a synthetic spectral line. The RW (proxy for EW) is clearly increasing with $\log gf$ (proxy for abundance). . . . .	14
2.5	Curve of growth for three different values of $\xi_{\text{micro}}$ . The EW is increasing with increasing $\xi_{\text{micro}}$ . . . . .	15
2.6	Overview of the minimization for FASMA. Credit: <a href="#">Andreasen et al. (2017a)</a> . . . . .	19

## LIST OF TABLES



## INTRODUCTION

Effective temperature ( $T_{\text{eff}}$ ), surface gravity ( $\log g$ ), and metallicity ( $[M/H]$ , where iron is normally used as a proxy) are fundamental atmospheric parameters necessary to characterise a single star, and to determine other indirectly fundamental parameters such as mass, radius, and age from stellar evolution models (see e.g. [Baraffe et al., 2015](#); [Dotter et al., 2008](#); [Girardi et al., 2000](#)). Precise and accurate stellar parameters are also essential in exoplanet searches. Planetary radius and mass are mainly found from transit lightcurve analysis and radial velocity analysis, respectively. The determination of the mass of the planet implies a knowledge of the stellar mass, while the measurement of the radius of the planet is dependent on our capability to derive the radius of the star (see e.g. [Ammler-von Eiff et al., 2009](#); [Torres et al., 2012, 2008](#)).

The derivation of precise stellar atmospheric parameters is not a simple task. Different approaches often lead to discrepant results (see e.g. [Lebzelter et al., 2012](#); [Santos et al., 2013](#); [Torres et al., 2010](#)). Interferometry is usually considered an accurate method for deriving stellar radii (see e.g. [Boyajian et al., 2012](#)); however, it is only applicable for bright nearby stars. Asteroseismology, on the other hand, reveals the inner stellar structure by observing the stellar pulsations at the surface. From asteroseismology it is possible to measure the surface gravity and mean density, and therefore to calculate mass and radius with high precision (see e.g. [Kjeldsen and Bedding, 1995](#)). However, for stars on the main sequence asteroseismic methods can typically only be applied to FG stars, since the oscillation modes of K and M dwarfs are likely too weak to be detected even with high precision spectroscopy or photometry. Moreover, the effective temperature is needed when applying asteroseismology in order to obtain the surface gravity and the mean density.

A crucial parameter for the indirect determination of stellar bulk properties is the  $T_{\text{eff}}$ . In that respect, the infrared flux method (IRFM) has proven to be reliable for FGK dwarf and subgiant stars. For higher accuracy the IRFM needs a priori knowledge of the bolometric flux, reddening, surface gravity, and stellar metallicity (Blackwell and Shallis, 1977; Casagrande et al., 2010; Ramírez and Meléndez, 2005).

Finally, the use of high resolution spectroscopy along with stellar atmospheric models is an extensively tested method that allows the derivation of the fundamental parameters of a star (see e.g. Santos et al., 2013; Valenti and Fischer, 2005). The procedure depends on the quality of the spectra, their resolution, and wavelength region. A fit to the overall spectrum can be applied for all spectral resolutions, but are often time consuming (see e.g. Recio-Blanco et al., 2006; Tsantaki et al., 2014). For resolutions higher than  $\lambda/\Delta\lambda \sim 20\,000$  we can apply the equivalent width (EW) method (see e.g. Andreasen et al., 2017a; Tsantaki et al., 2013, for details). However, while the latter approach is often faster than the synthetic fitting, it requires higher quality spectra, and the star to be slow rotating (below 10 km/s to 15 km/s).

Standard procedures are often used to derive stellar atmospheric parameters from high quality spectra in the optical (see e.g. Sousa et al., 2008; Valenti and Fischer, 2005). With the advancement of high resolution near-infrared (NIR) instruments, we will now be able to use a similar technique to that used in the optical part of the spectrum (see e.g. Bensby et al., 2014; Meléndez and Barbuy, 1999; Mucciarelli et al., 2013; Sousa et al., 2008; Tsantaki et al., 2013). At the moment, the GIANO spectrograph installed at *Telescopio Nazionale Galileo* (TNG) is already available (Origlia et al., 2014), as is the *infrared Doppler instrument* (IRD) installed at the Subaru telescope (Kotani et al., 2014), *Calar Alto high-Resolution search for M dwarfs with Exoearths with Near-infrared and optical Échelle Spectrographs* (CARMENES) for the 3.5 m telescope at Calar Alto Observatory (Quirrenbach et al., 2014), and *iShell* at the *InfraRed Telescope Facility* (Rayner et al., 2012, 2016). Three new spectrographs are planned for the near future: 1) The *CRyogenic InfraRed Echelle Spectrograph Upgrade Project* (CRIRES+) at the *Very Large Telescope* (VLT) (Follert et al., 2014) with expected first light in 2017, 2) *un SpectroPolarimètre Infra-Rouge A Near-InfraRed Spectropolarimeter* (SPIRou) at *The Canada-France-Hawaii Telescope* (CFHT) (Artigau et al., 2014; Delfosse et al., 2013) with expected first light in 2017 as well, and 3) *Near Infrared Planet Searcher* NIRPS at the ESO 3.6 m telescope in La Silla (Conod et al., 2016). The spectral resolutions for these spectrographs range between 50 000 and 100 000.

With the advance of the next generation NIR spectrographs, we are still preparing the data analysis of stellar spectra, in particular how to get reliable atmospheric parameters (see e.g. Andreasen et al., 2016; Lindgren et al., 2016; Önehag et al., 2012). The analysis of stellar spectra is well understood for FGK stars in the optical part of the spectrum, however some work still needs to be

done for the NIR part.

We continue our series of studies to explore the use of the NIR domain to derive stellar parameters for FGK and M stars. In particular, here we analyse the atlas of Arcturus and the spectrum of 10 Leo. For the analysis we use the iron line list presented in [Andreasen et al. \(2016\)](#) (referred to as Paper I). In Paper I we successfully tested our method on a slightly hotter star than the Sun, while in this work we aim to test the method on cooler stars. The strength of the NIR domain over the optical becomes clear when we move towards the cooler stars. Here we see less continuum depression and line blending due to in particular molecular features. Moreover, the cooler stars emit more light in the NIR domain than the optical, and with the lightest stars being intrinsically faint, we thus obtain the majority of the flux here.

## 1.1 Planet host stars

With the present diversity of exoplanets it becomes increasingly important to get an accurate and precise characterization of the planets in order to study them in samples and on an individual level. An accurate and precise characterization can give us an idea whether the planet is rocky, composed of water or gaseous.

## 1.2 Atmospheric parameters



## THEORY

To encompass all theory regarding stellar structure, evolution, and their atmosphere is far beyond the scope of this thesis. Rather the theory needed is presented below with highlights on the most important aspects.

### 2.1 Stellar structure

The structure of a non-rotating spherical stars can be described by five rather simple differential equations (see e.g. [Kippenhahn and Weigert, 1994](#)) presented below:

#### 1. Equation of Continuity

Relation between the mass,  $m$ , the density,  $\rho$ , at a symmetric shell at radius  $r$

$$\frac{\partial r}{\partial m} = \frac{1}{4\pi r^2 \rho}. \quad (2.1)$$

#### 2. Equation of Hydrostatic Equilibrium

The equation of hydrostatic equilibrium shows how a star in equilibrium is balanced between two forces. The inward force from gravity and the outward force from pressure,  $P$ ,

$$\frac{\partial P}{\partial m} = -\frac{Gm}{4\pi r^4}. \quad (2.2)$$

When working with asteroseismology a time dependent perturbation to this equation is added (see e.g. [Aerts et al., 2010](#), for a thorough discussion). However, this term is neglected here.

### 3. Equation of Energy Conservation

The equation of energy conservation shows how the energy is produced and lost throughout the star.

$$\boxed{\frac{\partial l}{\partial m} = \varepsilon - \varepsilon_\nu + \varepsilon_g}, \quad (2.3)$$

where  $\varepsilon$  is the energy production in the centre of the star,  $\varepsilon_\nu$  is the energy lost by neutrinos which is always positive,  $\varepsilon_g$  is a source function of time-dependent terms, and  $l$  is the luminosity at  $m$ .  $\varepsilon_g$  comes from the fact that non-stationary shells can change its internal energy, and thus exchange mechanical energy with neighbouring shells.

### 4. Equation of Energy Transport

Energy transportation throughout the star is described with the following equation

$$\boxed{\frac{\partial T}{\partial m} = -\frac{GmT}{4\pi r^4 P} \nabla_{\text{rad}}}, \quad (2.4)$$

where  $\nabla_{\text{rad}}$  is the radiative temperature gradient, and  $T$  is the temperature. The value of the temperature gradient compared to the radiative temperature gradient tells if the energy is transported by convection or radiation. In our Sun the outer layer are convective while the inner layer are radiative.

### 5. Equation of Chemical Composition

In this last equation we see the evolution of an element,  $X_i$ , when it reacts with other elements with reaction rates  $r_{ji}$  and  $r_{ik}$

$$\boxed{\frac{\partial X_i}{\partial t} = \frac{m_i}{\rho} \left( \sum_j r_{ji} - \sum_k r_{ik} \right)}. \quad (2.5)$$

Note that this is the only time-dependent equation of the five presented.

These five fundamental equations are implemented in stellar evolutionary codes, which we will use in later chapters. The many different codes that exist

take other things into account, e.g the star can rotate, and it may not always be in hydrostatic equilibrium (this is important if we want our star to pulsate). For simplicity we have only presented time-dependence in the Equation of Chemical Composition since timescales of rotation, pulsations, and activity are much shorter than the long timescale found in chemical composition changes.

## 2.2 Stellar atmosphere

Much of this Section is inspired by [Gray \(2005\)](#). While all the figures here were made by the author of this thesis, most of them can be found in [Gray \(2005\)](#) as well.

Stellar atmospheres are rather complicated. This is where the light produced in the interior of the stars are released. However, the atmosphere of a star is not transparent to all light, and some of the light is absorbed in the atmosphere and later emitted in a random direction. The different elements in the atmosphere is the reason for absorbing light at specific wavelength. The strength of the absorption depends on the physical conditions in the atmosphere, the effective temperature ( $T_{\text{eff}}$ ), the pressure/gravity ( $\log g$ ), the overall metallicity ( $[\text{Fe}/\text{H}]$ ), the specific abundance of a given element if different from the overall metallicity ( $A$ ), and the atomic characteristics of the transition coursing the absorption line.

It is important to know the fraction of atoms excited to the  $n$ th energy level,  $N_n$ . This fraction is proportional to the statistical weight  $g_n$  and the Boltzmann factor and is described as:

$$\boxed{\frac{N_n}{N} = \frac{g_n}{u(T)} 10^{-\theta\chi_n}} \quad \text{Boltzmann}$$

This equation is also called the Boltzmann equation. Here  $N$  is the total number of atoms per unit volume,  $u(T) = \sum g_i e^{-\chi_i/kT}$  is the partition function,  $k$  is Boltzmann's constant,  $T$  is the temperature, and  $\chi_n$  is the excitation potential for the lower energy level.

While atoms can get excited following Boltzmann's equation above, they can also get ionised. The ionisation for a collision dominated gas (which is a good approximation for FGKM stars), the ratio of neutral atoms to single ionised atoms is described by the Saha equation:

$$\boxed{\frac{N_1}{N_0} P_e = \frac{(2\pi m_e)^{3/2} (kT)^{5/2}}{h^3} \frac{2u_1(T)}{u_0(T)} e^{-I/kT}} \quad \text{Saha}$$

here  $m_e$  is the electron mass,  $h$  is Planck's constant, and  $I$  is the ionisation potential of the neutral atom.

The atomic lines are characterised by few quantum mechanical descriptors.

- The wavelength describes between which energy levels there is a transition, i.e. at which wavelength the light is absorbed.
- The ionisation state, i.e. is it a atom element absorbing or a ionised atom.
- The excitation potential. This gives an idea how deep in the atmosphere a line is formed. If  $\chi$  is high, then higher temperatures (i.e. higher random motion and more collisions between the atoms) is required for forming the absorption line. These higher temperatures are found deeper in the atmosphere.
- The oscillator strength,  $\log gf$ , is related to the atomic transition probability.
- The damping coefficients, is a natural damping (also known as radiation damping) caused by the uncertainty of lifetime in an energy level according to Heisenberg's uncertainty principle. This is related to a uncertainty in the energy level and thus a natural broadening is introduced.

These are essential to know from either theoretical calculations or experiments. The oscillator strength is a quantity that is difficult to measure, and this is often changed when absorption lines are matched with real observations of e.g. the Sun. This is a way of calibrating a line list and will be described in detail in Section 2.3.1 on page 15.

It is important to mention that one of the main differences between absorption lines in optical and near-infrared is the excitation potential. The energy levels of an atom gets denser packed as the energy level increase. This means that the difference in energy levels gets smaller, or in other words it gets redder. Therefore, the NIR absorption lines are, in average, produced at higher excitation potentials, which means in the deeper layers of the atmosphere.

### 2.2.1 Atmosphere models

In order to derive abundances or calculate a synthetic spectrum, two main things are needed: 1) An atmosphere model, and 2) a radiative transfer code that solves the equations above. There are different atmosphere models available. Throughout this thesis the ATLAS9 model atmosphere are used by Kurucz (1993). Other mentionable atmosphere models includes MARCS models (Gustafsson et al., 2008) and the PHOENIX models (Husser et al., 2013). An atmosphere model is a file with typically 72 layers. Each layer includes physical quantities such as temperature, gas and electron pressure, the optical depth, etc. The models can be calculated on the fly, but it is common practise to pre-calculate a grid of atmosphere models at certain  $T_{\text{eff}}$ ,  $\log g$ , and  $[\text{Fe} / \text{H}]$ . A specific atmosphere model is then obtained from this grid by interpolating from nearest neighbours. The interpolation code used throughout this work



includes the four nearest neighbours in the  $T_{\text{eff}}$ -space, and the two nearest neighbours in both the  $\log g$ - and  $[\text{Fe} / \text{H}]$ -space, in total  $4 \times 2 \times 2 = 16$  atmosphere models to generate a single interpolated atmosphere model.

### 2.2.2 Radiative transfer code - MOOG

As mentioned above, a radiative transfer code is needed to solve the equations above. There are many different codes that does this. Here the MOOG code is used (Snedden, 1973). This code has different drivers, only some are used here.

- Derive a theoretical equivalent width (see Section 2.2.3 for details) for a given star, i.e. atmosphere model with a given set of atmospheric parameters.
- Derive line abundance from a measured equivalent width for a given model atmosphere.
- Calculate a synthetic spectrum for a given model atmosphere and atomic line list.
- Calculate the curve-of-growth for an atomic line.

There exists other drivers as well, but these are the ones used here. Some only for visualizing the figures below.

### 2.2.3 The equivalent width

Measuring the equivalent width (EW) of spectral lines are important for some analysis of stellar spectra. The EW is a measure of the strength of the line, and dependent on the atmospheric conditions in where the spectral line is formed, such as  $T_{\text{eff}}$ ,  $\log g$ ,  $[\text{Fe} / \text{H}]$ , and  $\xi_{\text{micro}}$ .

The EW is mathematically described as integrating over the entire line, and assign this area to a rectangle from 0 to the continuum flux ( $F_c$ ) with the width, EW. This is illustrated in Figure 2.1 on the following page and the equation below:

$$EW = \int_0^\infty \frac{F_c - F(\lambda)}{F_c} d\lambda, \quad (2.6)$$

where  $\lambda$  is the wavelength. This integral is assuming there is only one single line, hence the integral is over all wavelength. In practice the integral is calculated in small windows around a spectral line. See Section 2.3.2 on page 16 for more details on how this is performed in practice. The unit of the EW is the same as the wavelength used. Throughout this thesis we will use Ångström ( $1\text{\AA} = 0.1\text{ nm}$ ) for the wavelength, and mÅ for the EW.

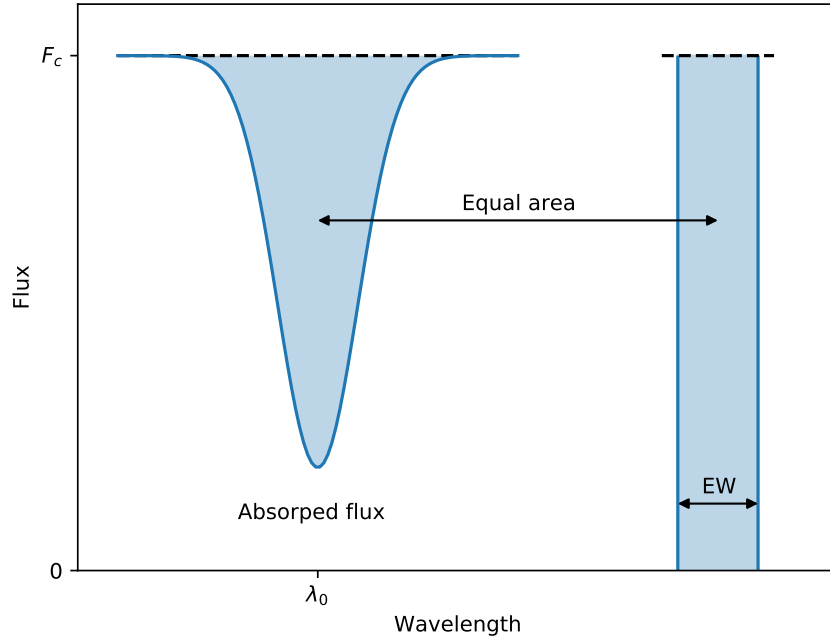


**Figure 2.1:** An absorption line centred at  $\lambda_0$  normalised at the flux level  $F_c$ . The area of the absorption line to the left is equal to the blue shaded area in the rectangle to the right with width EW.

### 2.2.3.1 Temperature dependence

As mentioned above the EW depends on the atmospheric parameters. The dependence on  $T_{\text{eff}}$  is the strongest dependence. At low  $T_{\text{eff}}$  neutral elements, say Fe I, are the strongest lines as the number of ionised atoms are too small to contribute significantly to the EW. This is the result the Saha equation. As  $T_{\text{eff}}$  increases Fe I is converted into ionised Fe II. Slowly, as the number of Fe I decreases so does the EW, and likewise as the number of Fe II increases so does the EW. This goes on until second ionised atoms, Fe III, are formed and the same situation arise again. This is illustrated in Figure 2.2 on the facing page where the EW of two iron lines, one neutral and one ionised, are plotted against  $T_{\text{eff}}$ . These two lines have similar EW in the Sun: 46.2 mÅ and 53.9 mÅ for the Fe I and Fe II line respectively.

### 2.2.3.2 Pressure dependence

Pressure dependence in the stellar atmosphere can be related to the gravity dependence. There are many ways to measure the pressure, and thus the

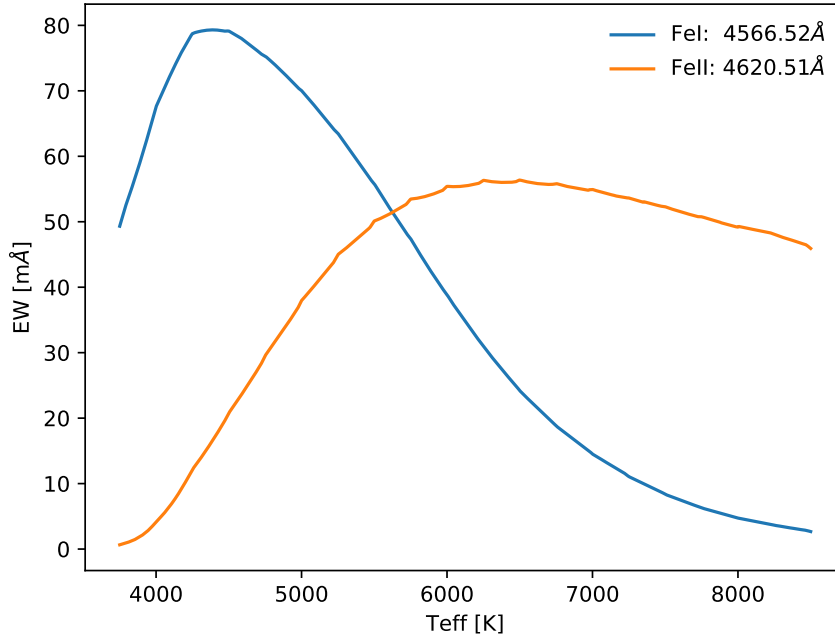


**Figure 2.2:** The EW for a Fe I and Fe II line with increasing  $T_{\text{eff}}$ . The two lines have similar EW in the Sun and are found in the optical part of the spectrum.

gravity which is what is ultimately the goal with the measurement of  $\log g$ . Below are listed some of the most common methods to measure  $\log g$  from spectroscopy.

- **Continuum:** The Balmer jump is the only continuum feature sensitive enough to estimate the  $\log g$ .
- **Hydrogen lines:** Hydrogen profiles are pressure sensitive and can therefore be used to estimate  $\log g$ . However, the gravity dependence rapidly diminishes for temperatures above 10 000 K.
- **Other strong lines:** There exists other strong lines with pressure-broadened wings such as the Ca II H and K lines. These are better for cooler stars than the hydrogen lines described above.
- **Weak lines:** By comparing two stages of ionisation for the same element it is possible to obtain  $\log g$  using weaker or modestly strong lines.

In this thesis weak lines are used to measure  $\log g$ . More specifically a comparison between Fe I and Fe II lines are used. For FGK stars, as the atmosphere

contracts (i.e.  $\log g$  increases) the pressure likewise increases, which in turn means that both the gas pressure,  $P_g$ , and electron pressure,  $P_e$ , increases. Since hydrogen is the main electron contributor, but not fully ionised for these stars, the electron pressure is much smaller than the gas pressure. The gas pressure follows a simply empirical approximation with gravity:

$$P_g \simeq \text{constant } g^{2/3}, \quad (2.7)$$

This needs to be expanded and completed!

where  $g$  is the gravity.

In Figure 2.3 on the next page is shown how the Fe II line used previously changes with  $\log g$ . The curve of growth is shown in the upper panel, while a synthetic spectrum for each  $\log g$  is presented in the lower left panel. It is clear that the ionised line is sensitive to  $\log g$  as shown in the lower right panel, where the correlation between the abundance and  $\log g$  is 0.40. This is expected as can be seen in Gray (2005, Table 16.1). There is used  $\delta \log A / \delta \log g$  as an indicator, and for neutral elements the correlation is much weaker. It is important to note that the correlation does change with  $T_{\text{eff}}$  and the element used.

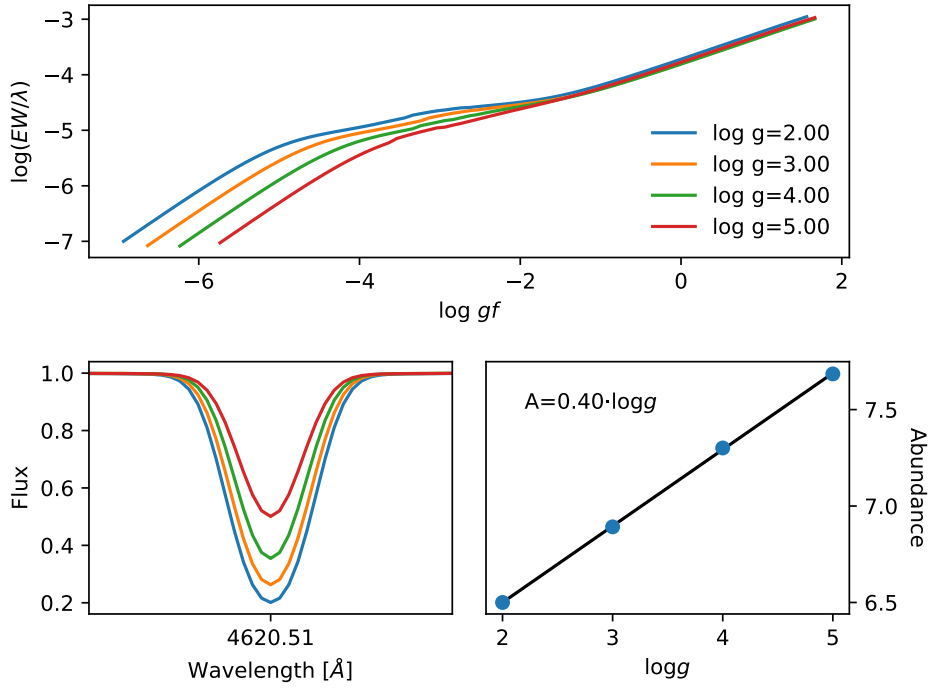
### 2.2.3.3 Abundance dependence

The abundance of a given element obviously has an effect on the EW. The more abundant an element is, the more photons can be absorbed thus increasing the EW. However, the relationship is not strictly linear. For weak lines (GIVE RANGE) EW is approximately linear with the abundance, however it reaches a plateau where the core of the line saturates. In this regime the EW only increases slowly, until the absorption "spills" into the wings and the increase is again linear. However, for these strong lines the profile is no longer Gaussian. The curve of growth for the same Fe I line used in Figure 2.2 on the preceding page is shown in Figure 2.4 on page 14. Instead of EW it is common to use the reduced EW,  $\log(EW/\lambda)^1$ , which we will use more later. Instead of the abundance of a line, the oscillator strength,  $\log gf$ , is used.

### 2.2.3.4 Microturbulence

Small-scale motion, that is motion of material at length scales small compared to the unit optical depth, are called microturbulence,  $\xi_{\text{micro}}$ . This is not to be confused with macroturbulence, which is motion of material at scales larger than the unit optical depth. The latter is associated with granulation and will not be discussed further in this thesis.  $\xi_{\text{micro}}$  comes into play when looking at the curve of growth for saturated lines (i.e. between green and red points in

<sup>1</sup> The reduced EW is useful since it normalises Doppler-dependent phenomena, such as microturbulence and thermal broadening.



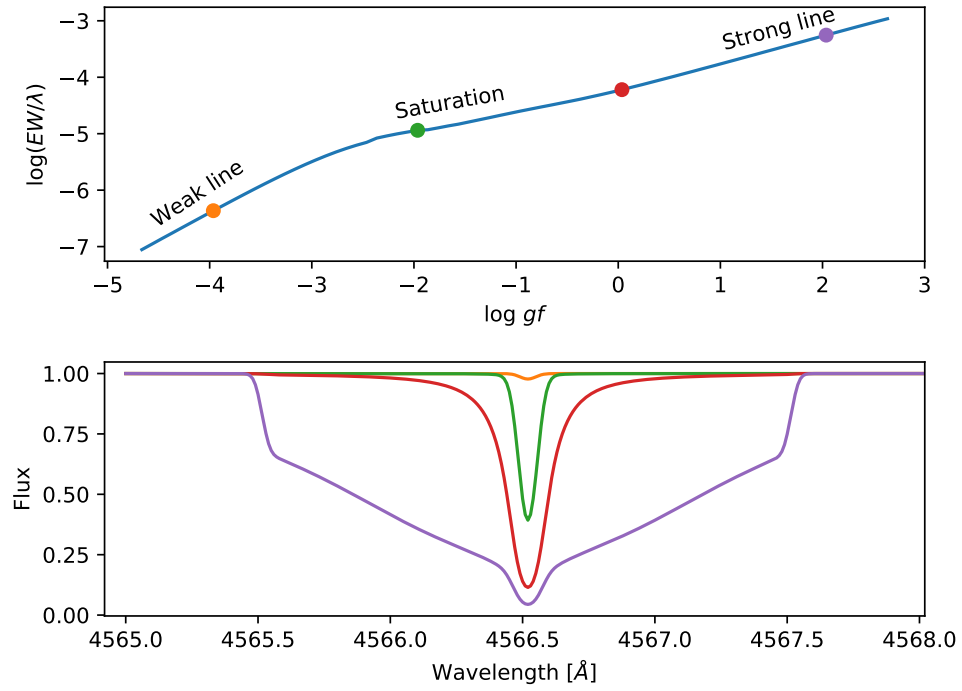
**Figure 2.3:** Upper panel: Curve of growth for same Fe II used in Figure 2.2 on page 11 for four different  $\log g$  values. Here it is the weak lines mostly affected by the change in  $\log g$ . Lower left panel: Synthetic spectra of the same line. The colour scale is the same. Lower right: The abundance for the line at different  $\log g$ . A strong correlation (0.40) is seen.

Figure 2.4 on the following page). If no  $\xi_{\text{micro}}$  is assumed, then the measured abundance is higher than predicted by models based on thermal and damping broadening alone. In Figure 2.5 on page 15 is shown three curves of growth with  $\xi_{\text{micro}} = 0.5 \text{ km/s}, 2.5 \text{ km/s}, 5.0 \text{ km/s}$ . As  $\xi_{\text{micro}}$  increases, so does the EW and hence the abundance.

The broadening of an absorption line measured by the shift in wavelength,  $\Delta\lambda$ , when  $\xi_{\text{micro}}$  is included is defined as:

$$\Delta\lambda = \frac{\lambda_0}{c} \sqrt{\frac{2kT}{m} + \xi_{\text{micro}}^2}, \quad (2.8)$$

where  $c$  is the speed of light,  $\lambda_0$  is the rest wavelength of the given line,  $k$  is Boltzmann's constant,  $T$  is the temperature, and  $m$  is the mass of the atom. Setting  $\xi_{\text{micro}} = 0 \text{ km/s}$ , we end up with thermal broadening.



**Figure 2.4:** Upper panel: Curve of growth of the same Fe I line as used in Figure 2.2 on page 11. Four points are marked which is shown in the lower panel as a synthetic spectral line. The RW (proxy for EW) is clearly increasing with  $\log gf$  (proxy for abundance).

### 2.3 Stellar parameters for FGK stars - the EW method

In this section, the process from a spectrum to atmospheric parameters will be explained in details. There are two classic methods, synthetic fitting and curve-of-growth analysis.

The synthetic fitting method is in simple terms a comparison between the observed spectrum and a synthetic spectrum, which is either calculated on the fly like SME (Valenti and Piskunov, 1996), or using a pre-calculated grid. By analysing the  $\chi^2$  the synthetic spectrum that best match the observed spectrum can be found. This technique works for all ranges of spectral resolutions and can work for many rotational profiles as well (see e.g. Tsantaki et al., 2017). However, this method is often time-consuming compared to the curve-of-growth analysis.

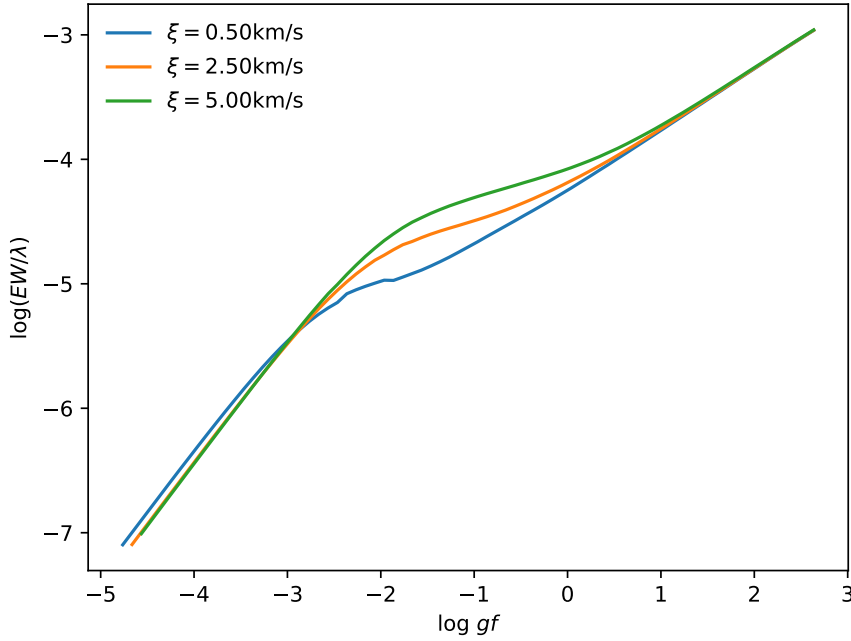


**Figure 2.5:** Curve of growth for three different values of  $\xi_{\text{micro}}$ . The EW is increasing with increasing  $\xi_{\text{micro}}$ .

### 2.3.1 Line list and atomic data

As mentioned above, the atomic data of the absorption lines are required. These data can be found in a database such as *The Vienna Atomic Line Data Base* (VALD) (Kupka et al., 2000; Piskunov et al., 1995). For compiling a usable iron line list, all theoretical transitions in a given wavelength range are requested from VALD. In the near-infrared (NIR), YJHK bands, there are several thousands of theoretical transitions. The EWs are measured (see Section 2.3.2 on the following page) for all these lines using a solar spectrum (Hinkle et al., 1995, is used here). Here there are four possible outcomes. 1) A line can not be measured and is thus discarded, 2) the EW of the line is weak (below 5 mÅ) to be reliable, 3) the EW of the line is too strong (above 150 mÅ) and the line shows non-linear behaviour in the curve-of-growth (see Figure 2.4 on the preceding page), or 4) the EW of the line is between the two limits and is then added to the final line list.

After removing lines which EW is outside the range of EW mentioned above, it is good practise to have a visual inspection. Here one should look for severe line blending with other absorption lines which might prove prob-

lematic and unreliable measurements of the EW. If the reference spectrum used, here for the Sun, is not corrected for telluric lines, it is also a good idea to remove lines which exists amidst forest of telluric lines, as these absorption lines might fall on the telluric lines, if the star observed has a different radial velocity (RV).

When blended lines and otherwise lines which shows strange features (can be in a forest of telluric lines), the last step is to calibrate the atomic data. As mentioned above, this is done by changing the  $\log gf$  value for a given line, until it has the desired determined abundance. In this case, an iron line should have the abundance of 7.47 using the values from [Gonzalez and Laws \(2000\)](#), when using a solar atmosphere model. There is a simple anti-correlation between the determined abundance from the measured EW and the  $\log gf$ , so a simple bisector minimization can be used to find the best  $\log gf$ . It is important to calibrate the  $\log gf$  when changing the version of MOOG (or if other radiative transfer codes are used), the atmosphere model and version of those, and even the interpolation of the atmosphere models. These changes in  $\log gf$  should be minor compared to the change from the VALD database and those we arrive at when calibrated for the Sun.

### 2.3.2 Measuring EW

There are two ways to measure the EW of an absorption line, manual or automatic. Both of these methods are used here. There are advantages and disadvantages for both method. For the manual, an advantage is that we can inspect the lines and try to measure lines in different ways (which is useful if it is blended). Disadvantages are that it is very time consuming, and it is prone to errors, as a measurement might change drastically by the eyes measuring it. Even for the same person, the measurement can change. By mentioning the advantages and disadvantages of the manual method, it should be clear that the advantages and disadvantages of the automatic method is the opposite of those. Especially the time to measure the lines is order of magnitudes faster, which is crucial when dealing with more than a handful of spectra.

When a line is measurement by hand (manual) it is done using the `splot` command in IRAF. Here the deblending mode is used whenever necessary. It is often necessary to fit one spectral lines with several Gaussians, as neighbouring lines might contaminate the line of interest slightly.

When a line is measurement automatically it is done with ARES ([Sousa et al., 2015, 2007](#)). When using ARES it is important to use a correct value of the `rejt` parameter. This parameter is used for placing the continuum level, and is thus directly related to the final measurement EW. It is difficult to get this parameter right, however the newest version of ARES has the option to analyse a few absorption free regions and measure the S/N. The `rejt` is then



calculated as:

$$rejt = 1 - \frac{1}{S/N}.$$

As all, or as many as possible, the lines in the line list have measured EWs, the next step in determining the atmospheric parameters is to determine the abundance for each line and imposing excitation and ionization balance.

### 2.3.3 Excitation and ionization balance

With the measured EWs for all the lines in the line list, we choose an atmosphere model to determine the abundances. If there is no prior knowledge of the star it is common simple choose a solar atmosphere model as a starting point. Next the correlation between the abundances and the reduced EWs, and the abundances and the excitation potential is calculated. If there is a correlation it means the atmosphere model used is wrong. Moreover, we also have to check if the mean abundance of Fe I and Fe II lines are equal, and last if mean abundance of the Fe I lines is equal to the unput  $[Fe/H]$  of the atmosphere model<sup>2</sup>. If one of these four criteria does not pass, then the atmosphere model is wrong, and we have to search for a new one. A common way to do this, is by combining the indicators into a scalar value:

$$f(\{T_{\text{eff}}, \log g, [Fe/H], \xi_{\text{micro}}\}) = \sqrt{a_{\text{EP}}^2 + a_{\text{RW}}^2 + \Delta Fe^2}, \quad (2.9)$$

where  $a_{\text{EP}}$  is the correlation between abundances and excitation potential,  $a_{\text{RW}}$  is the correlation between abundances and reduced EW, and  $\Delta Fe$  is the difference between the mean abundances of Fe I and Fe II. This scalar function can be minimized using standard minimization procedures as the simplex downhill among others. However, there is another approach that takes into the account the information stored in these indicators. For example, if  $a_{\text{EP}}$  is positive it means  $T_{\text{eff}}$  has to be increased by an amount correlated by the numerical value of  $a_{\text{EP}}$ . In the same way, a non-zero  $a_{\text{RW}}$  means  $\xi_{\text{micro}}$  has to be changed, and  $\Delta Fe$  is an indicator for  $\log g$ . In the end it is a vector function being minimized which are more difficult, however we are not minimizing this using standard mathematical methods, but rather using the physical knowledge. This minimization is useless for anything else, but it is excellent for this. The vector function has the form:

$$f(\{T_{\text{eff}}, \log g, [Fe/H], \xi_{\text{micro}}\}) = \{a_{\text{EP}}, a_{\text{RW}}, \Delta Fe, Fe I\}. \quad (2.10)$$

In each iteration where convergence is not reached, the input metallicity is changed to that of the mean output metallicity using the Fe I lines. The

<sup>2</sup> We use Fe I instead of Fe II lines for this, since they are more numerous.

minimization is depicted in Figure 2.6 on the facing page. This minimization is written in the Python programming language and is also a wrapper around both ARES and MOOG. The entire package is called FASMA<sup>3</sup> (Andreasen et al., 2017a; Tsantaki et al., 2017). FASMA is able to fix one or all of the four atmospheric parameters, and when it reach convergence it checks if there are any outliers in the abundances. These will be removed, either all at once, all iteratively, meaning that after removing the outliers the minimization is restarted at the previous best parameters, and this process is continued until there can be removed no other outliers, or last is removing one outlier iteratively. An optical line list like the ones by Sousa et al. (2008); Tsantaki et al. (2013) have been tested thoroughly and it is safe to remove a larger amount of lines and still obtain reliable parameters. However, with a less tested line list, like the one by Andreasen et al. (2016) (and refined in Andreasen et al. (2017b)), one should remove outliers more carefully, and it is recommended that one outlier is removed iteratively.

In Figure 2.6 on the next page there is a flag with *autofixvt*. This was an option introduced since we see that some spectra does not converge, however the usual way to proceed is to fix the  $\xi_{\text{micro}}$ . This is done at the end of the minimization if the  $\xi_{\text{micro}}$  value is close to either 0km/s or 5km/s and  $|a_{\text{RW}}| > 0.050$ . When fixing  $\xi_{\text{micro}}$  with FASMA, its value is changed in each iteration following a simple empirical relation:

$$vt = \begin{cases} 6.935 \cdot 10^{-4} T_{\text{eff}} - 0.348 \log g - 1.437 & \text{For } \log g \geq 3.95 \\ 2.72 - 0.457 \log g + 0.072 \cdot [\text{Fe} / \text{H}] & \text{For } \log g < 3.95, \end{cases} \quad (2.11)$$

where the first case is from Tsantaki et al. (2013) and the latter case is from Adibekyan et al. (2015).

Last there is an option, *refine*. This apply more strict criteria for the indicators to reach convergence, thus making the minimization less sensitive to the initial guess since it could otherwise reach convergence from one "side" of the parameter space. The default criteria are:

$$a_{\text{EP}} = 0.001$$

$$a_{\text{RW}} = 0.003$$

$$\Delta\text{Fe} = 0.001.$$

The criteria for  $a_{\text{RW}}$  is not as strict as  $a_{\text{EP}}$  since this indicator can change rapidly with small changes in  $\xi_{\text{micro}}$ , thus a very strict criteria might never lead to convergence. Convergence is reached once all of the above criteria are met, and the input and output metallicity are identical. If one or more of the parameters are fixed, the corresponding criterium is simply set to 0 and effectively ignored, thus not changing the parameter.

---

<sup>3</sup> Greek for spectrum

For each iteration, the change to be applied for the atmospheric parameters are defined by adding the following:

$$T_{\text{eff}} : 2000 \text{ K} \cdot a_{\text{EP}} \quad (2.12)$$

$$\zeta_{\text{micro}} : 1.5 \text{ km/s} \cdot a_{\text{RW}} \quad (2.13)$$

$$\log g : -\Delta\text{Fe} \quad (2.14)$$

to each parameter. Note again that metallicity is simply changed to the the output metallicity of the previous iteration. These are empirical relations. Note that by changing e.g.  $T_{\text{eff}}$  not only is  $a_{\text{EP}}$  affected, but the other indicators as well. So there is a interdependency between the parameters, however this is ignored by FASMA as it is not a simple problem to solve. The stepping presented above is choised to rapidly reach convergence, without causing problems for the interdependency.

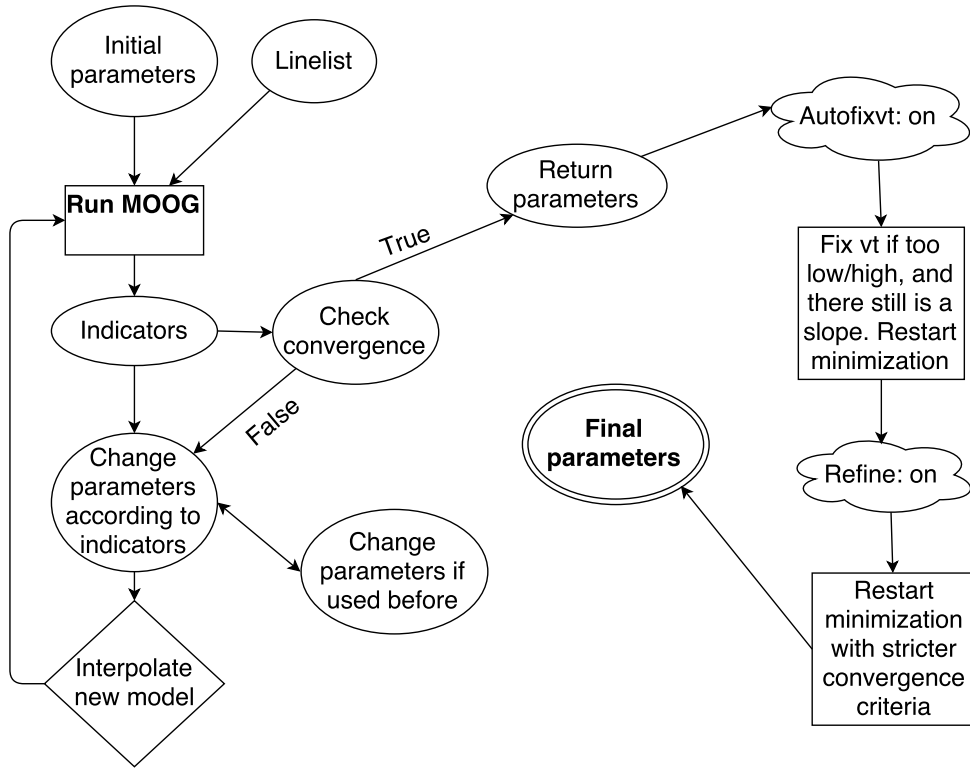


**Figure 2.6:** Overview of the minimization for FASMA. Credit: [Andreasen et al. \(2017a\)](#).



## BIBLIOGRAPHY

- Adibekyan, V. Z., Benamati, L., Santos, N. C., Alves, S., Lovis, C., Udry, S., Israelian, G., Sousa, S. G., Tsantaki, M., Mortier, A., Sozzetti, A., and De Medeiros, J. R.: 2015, *MNRAS* **450**, 1900
- Aerts, C., Christensen-Dalsgaard, J., and Kurtz, D. W.: 2010, *Asteroseismology*
- Ammler-von Eiff, M., Santos, N. C., Sousa, S. G., Fernandes, J., Guillot, T., Israelian, G., Mayor, M., and Melo, C.: 2009, *A&A* **507**, 523
- Andreasen, D. T., Sousa, S. G., Delgado Mena, E., Santos, N. C., Tsantaki, M., Rojas-Ayala, B., and Neves, V.: 2016, *A&A* **585**, A143
- Andreasen, D. T., Sousa, S. G., Tsantaki, M., Teixeira, G. D. C., Mortier, A., Santos, N. C., Suarez-Andres, L., Delgado-Mena, E., and Ferreira, A. C. S.: 2017a, *ArXiv e-prints*
- Andreasen, D. T., Sousa, S. G., Tsantaki, M., Teixeira, G. D. C., Mortier, A., Santos, N. C., Suárez-Andrés, L., Delgado Mena, E., and Ferreira, A. C. S.: 2017b, *A&A* **585**, A143
- Artigau, É., Kouach, D., Donati, J.-F., Doyon, R., Delfosse, X., Baratchart, S., Lacombe, M., Moutou, C., Rabou, P., Parès, L. P., Mischeau, Y., Thibault, S., Reshetov, V. A., Dubois, B., Hernandez, O., Vallée, P., Wang, S.-Y., Dolon, F., Pepe, F. A., Bouchy, F., Striebig, N., Hénault, F., Loop, D., Saddlemyer, L., Barrick, G., Vermeulen, T., Dupieux, M., Hébrard, G., Boisse, I., Martioli, E., Alencar, S. H. P., do Nascimento, J.-D., and Figueira, P.: 2014, in *Society of Photo-Optical Instrumentation Engineers (SPIE) Conference Series*, Vol. 9147 of *Society of Photo-Optical Instrumentation Engineers (SPIE) Conference Series*, p. 15
- Baraffe, I., Homeier, D., Allard, F., and Chabrier, G.: 2015, *A&A* **577**, A42
- Bensby, T., Feltzing, S., and Oey, M. S.: 2014, *A&A* **562**, A71
- Blackwell, D. E. and Shallis, M. J.: 1977, *MNRAS* **180**, 177

- Boyajian, T. S., von Braun, K., van Belle, G., McAlister, H. A., ten Brummelaar, T. A., Kane, S. R., Muirhead, P. S., Jones, J., White, R., Schaefer, G., Ciardi, D., Henry, T., López-Morales, M., Ridgway, S., Gies, D., Jao, W.-C., Rojas-Ayala, B., Parks, J. R., Sturmann, L., Sturmann, J., Turner, N. H., Farrington, C., Goldfinger, P. J., and Berger, D. H.: 2012, *ApJ* 757, 112
- Casagrande, L., Ramírez, I., Meléndez, J., Bessell, M., and Asplund, M.: 2010, *A&A* 512, A54
- Conod, U., Blind, N., Wildi, F., and Pepe, F.: 2016, in *Society of Photo-Optical Instrumentation Engineers (SPIE) Conference Series*, Vol. 9909 of *Proceedings of the SPIE*, p. 990941
- Delfosse, X., Donati, J.-F., Kouach, D., Hébrard, G., Doyon, R., Artigau, E., Bouchy, F., Boisse, I., Brun, A. S., Hennebelle, P., Widemann, T., Bouvier, J., Bonfils, X., Morin, J., Moutou, C., Pepe, F., Udry, S., do Nascimento, J.-D., Alencar, S. H. P., Castilho, B. V., Martioli, E., Wang, S. Y., Figueira, P., and Santos, N. C.: 2013, in L. Cambresy, F. Martins, E. Nuss, and A. Palacios (eds.), *SF2A-2013: Proceedings of the Annual meeting of the French Society of Astronomy and Astrophysics*, pp 497–508
- Dotter, A., Chaboyer, B., Jevremović, D., Kostov, V., Baron, E., and Ferguson, J. W.: 2008, *ApJS* 178, 89
- Follert, R., Dorn, R. J., Oliva, E., Lizon, J. L., Hatzes, A., Piskunov, N., Reiners, A., Seemann, U., Stempels, E., Heiter, U., Marquart, T., Lockhart, M., Anglada-Escude, G., Löwinger, T., Baade, D., Grunhut, J., Bristow, P., Klein, B., Jung, Y., Ives, D. J., Kerber, F., Pozna, E., Paufigue, J., Kaeufl, H. U., Origlia, L., Valenti, E., Gojak, D., Hilker, M., Pasquini, L., Smette, A., and Smoker, J.: 2014, in *Society of Photo-Optical Instrumentation Engineers (SPIE) Conference Series*, Vol. 9147 of *Society of Photo-Optical Instrumentation Engineers (SPIE) Conference Series*, p. 19
- Girardi, L., Bressan, A., Bertelli, G., and Chiosi, C.: 2000, *A&A Supp.* 141, 371
- Gonzalez, G. and Laws, C.: 2000, *AJ* 119, 390
- Gray, D. F.: 2005, *The Observation and Analysis of Stellar Photospheres*, 3rd ed.
- Gustafsson, B., Edvardsson, B., Eriksson, K., Jørgensen, U. G., Nordlund, Å., and Plez, B.: 2008, *A&A* 486, 951
- Hinkle, K. H., Wallace, L., and Livingston, W.: 1995, in A. J. Sauval, R. Blomme, and N. Grevesse (eds.), *Laboratory and Astronomical High Resolution Spectra*, Vol. 81 of *Astronomical Society of the Pacific Conference Series*, p. 66

- Husser, T.-O., Wende-von Berg, S., Dreizler, S., Homeier, D., Reiners, A., Barman, T., and Hauschildt, P. H.: 2013, *A&A* 553, A6
- Kippenhahn, R. and Weigert, A.: 1994, *Stellar Structure and Evolution*, Springer-Verlag
- Kjeldsen, H. and Bedding, T. R.: 1995, *A&A* 293, 87
- Kotani, T., Tamura, M., Suto, H., Nishikawa, J., Sato, B., Aoki, W., Usuda, T., Kurokawa, T., Kashiwagi, K., Nishiyama, S., Ikeda, Y., Hall, D. B., Hodapp, K. W., Hashimoto, J., Morino, J.-I., Okuyama, Y., Tanaka, Y., Suzuki, S., Inoue, S., Kwon, J., Suenaga, T., Oh, D., Baba, H., Narita, N., Kokubo, E., Hayano, Y., Izumiura, H., Kambe, E., Kudo, T., Kusakabe, N., Ikoma, M., Hori, Y., Omiya, M., Genda, H., Fukui, A., Fujii, Y., Guyon, O., Harakawa, H., Hayashi, M., Hidai, M., Hirano, T., Kuzuhara, M., Machida, M., Matsuo, T., Nagata, T., Onuki, H., Ogihara, M., Takami, H., Takato, N., Takahashi, Y. H., Tachinami, C., Terada, H., Kawahara, H., and Yamamuro, T.: 2014, in *Society of Photo-Optical Instrumentation Engineers (SPIE) Conference Series*, Vol. 9147 of *Society of Photo-Optical Instrumentation Engineers (SPIE) Conference Series*, p. 14
- Kupka, F. G., Ryabchikova, T. A., Piskunov, N. E., Stempels, H. C., and Weiss, W. W.: 2000, *Baltic Astronomy* 9, 590
- Kurucz, R.: 1993, *ATLAS9 Stellar Atmosphere Programs and 2 km/s grid*. Kurucz CD-ROM No. 13. Cambridge, Mass.: Smithsonian Astrophysical Observatory, 1993. 13
- Lebzelter, T., Heiter, U., Abia, C., Eriksson, K., Ireland, M., Neilson, H., Nowotny, W., Maldonado, J., Merle, T., Peterson, R., Plez, B., Short, C. I., Wahlgren, G. M., Worley, C., Aringer, B., Bladh, S., de Laverny, P., Goswami, A., Mora, A., Norris, R. P., Recio-Blanco, A., Scholz, M., Thévenin, F., Tsuji, T., Kordopatis, G., Montesinos, B., and Wing, R. F.: 2012, *A&A* 547, A108
- Lindgren, S., Heiter, U., and Seifahrt, A.: 2016, *A&A* 586, A100
- Meléndez, J. and Barbuy, B.: 1999, *ApJS* 124, 527
- Mucciarelli, A., Pancino, E., Lovisi, L., Ferraro, F. R., and Lapenna, E.: 2013, *ApJ* 766, 78
- Önehag, A., Heiter, U., Gustafsson, B., Piskunov, N., Plez, B., and Reiners, A.: 2012, *A&A* 542, A33
- Origlia, L., Oliva, E., Baffa, C., Falcini, G., Giani, E., Massi, F., Montegriffo, P., Sanna, N., Scuderi, S., Sozzi, M., Tozzi, A., Carleo, I., Gratton, R., Ghinassi, F., and Lodi, M.: 2014, in *Society of Photo-Optical Instrumentation Engineers*

(SPIE) Conference Series, Vol. 9147 of *Society of Photo-Optical Instrumentation Engineers (SPIE) Conference Series*, p. 1

Piskunov, N. E., Kupka, F., Ryabchikova, T. A., Weiss, W. W., and Jeffery, C. S.: 1995, *A&A Supp.* 112, 525

Quirrenbach, A., Amado, P. J., Caballero, J. A., Mundt, R., Reiners, A., Ribas, I., Seifert, W., Abril, M., Aceituno, J., Alonso-Floriano, F. J., Ammler-von Eiff, M., Antona Jiménez, R., Anwand-Heerwart, H., Azzaro, M., Bauer, F., Barrado, D., Becerril, S., Béjar, V. J. S., Benítez, D., Berdiñas, Z. M., Cárdenas, M. C., Casal, E., Claret, A., Colomé, J., Cortés-Contreras, M., Czesla, S., Doellinger, M., Dreizler, S., Feiz, C., Fernández, M., Galadí, D., Gálvez-Ortiz, M. C., García-Piquer, A., García-Vargas, M. L., Garrido, R., Gesa, L., Gómez Galera, V., González Álvarez, E., González Hernández, J. I., Grözing, U., Guàrdia, J., Guenther, E. W., de Guindos, E., Gutiérrez-Soto, J., Hagen, H.-J., Hatzes, A. P., Hauschildt, P. H., Helmling, J., Henning, T., Hermann, D., Hernández Castaño, L., Herrero, E., Hidalgo, D., Holgado, G., Huber, A., Huber, K. F., Jeffers, S., Joergens, V., de Juan, E., Kehr, M., Klein, R., Kürster, M., Lamert, A., Lalitha, S., Laun, W., Lemke, U., Lenzen, R., López del Fresno, M., López Martí, B., López-Santiago, J., Mall, U., Mandel, H., Martín, E. L., Martín-Ruiz, S., Martínez-Rodríguez, H., Marvin, C. J., Mathar, R. J., Mirabet, E., Montes, D., Morales Muñoz, R., Moya, A., Naranjo, V., Ofir, A., Oreiro, R., Pallé, E., Panduro, J., Passegger, V.-M., Pérez-Calpena, A., Pérez Medialdea, D., Perger, M., Pluto, M., Ramón, A., Rebolo, R., Redondo, P., Reffert, S., Reinhardt, S., Rhode, P., Rix, H.-W., Rodler, F., Rodríguez, E., Rodríguez-López, C., Rodríguez-Pérez, E., Rohloff, R.-R., Rosich, A., Sánchez-Blanco, E., Sánchez Carrasco, M. A., Sanz-Forcada, J., Sarmiento, L. F., Schäfer, S., Schiller, J., Schmidt, C., Schmitt, J. H. M. M., Solano, E., Stahl, O., Storz, C., Stürmer, J., Suárez, J. C., Ulbrich, R. G., Veredas, G., Wagner, K., Winkler, J., Zapatero Osorio, M. R., Zechmeister, M., Abellán de Paco, F. J., Anglada-Escudé, G., del Burgo, C., Klutsch, A., Lizon, J. L., López-Morales, M., Morales, J. C., Perryman, M. A. C., Tulloch, S. M., and Xu, W.: 2014, in *Society of Photo-Optical Instrumentation Engineers (SPIE) Conference Series*, Vol. 9147 of *Society of Photo-Optical Instrumentation Engineers (SPIE) Conference Series*, p. 1

Ramírez, I. and Meléndez, J.: 2005, *ApJ* 626, 446

Rayner, J., Bond, T., Bonnet, M., Jaffe, D., Muller, G., and Tokunaga, A.: 2012, in *Ground-based and Airborne Instrumentation for Astronomy IV*, Vol. 8446 of *Proceedings of the SPIE*, p. 84462C

Rayner, J., Tokunaga, A., Jaffe, D., Bonnet, M., Ching, G., Connelley, M., Kokubun, D., Lockhart, C., and Warmbier, E.: 2016, in *Society of Photo-Optical*



- Instrumentation Engineers (SPIE) Conference Series*, Vol. 9908 of *Proceedings of the SPIE*, p. 990884
- Recio-Blanco, A., Bijaoui, A., and de Laverny, P.: 2006, *MNRAS* **370**, 141
- Santos, N. C., Sousa, S. G., Mortier, A., Neves, V., Adibekyan, V., Tsantaki, M., Delgado Mena, E., Bonfils, X., Israelian, G., Mayor, M., and Udry, S.: 2013, *A&A* **556**, A150
- Snedden, C. A.: 1973, *Ph.D. thesis*, THE UNIVERSITY OF TEXAS AT AUSTIN.
- Sousa, S. G., Santos, N. C., Adibekyan, V., Delgado-Mena, E., and Israelian, G.: 2015, *A&A* **577**, A67
- Sousa, S. G., Santos, N. C., Israelian, G., Mayor, M., and Monteiro, M. J. P. F. G.: 2007, *A&A* **469**, 783
- Sousa, S. G., Santos, N. C., Mayor, M., Udry, S., Casagrande, L., Israelian, G., Pepe, F., Queloz, D., and Monteiro, M. J. P. F. G.: 2008, *A&A* **487**, 373
- Torres, G., Andersen, J., and Giménez, A.: 2010, *Astronomy and Astrophysics Reviews* **18**, 67
- Torres, G., Fischer, D. A., Sozzetti, A., Buchhave, L. A., Winn, J. N., Holman, M. J., and Carter, J. A.: 2012, *ApJ* **757**, 161
- Torres, G., Winn, J. N., and Holman, M. J.: 2008, *ApJ* **677**, 1324
- Tsantaki, M., Andreasen, D. T., Teixeira, G. D. C., Sousa, S. G., Santos, N. C., Delgado-Mena, E., and Bruzual, G.: 2017, *MNRAS* **555**, A150
- Tsantaki, M., Sousa, S. G., Adibekyan, V. Z., Santos, N. C., Mortier, A., and Israelian, G.: 2013, *A&A* **555**, A150
- Tsantaki, M., Sousa, S. G., Santos, N. C., Montalto, M., Delgado-Mena, E., Mortier, A., Adibekyan, V., and Israelian, G.: 2014, *A&A* **570**, A80
- Valenti, J. A. and Fischer, D. A.: 2005, *ApJS* **159**, 141
- Valenti, J. A. and Piskunov, N.: 1996, *A&A Supp.* **118**, 595